Research Article Vol. 30, No. 1 / 3 Jan 2022 / Optics Express 166
Optics EXPRESS

Calibration method for an extended depth-of-field microscopic structured light system

LIMING CHEN,[1] XIAOWEI HU,[2] AND SONG ZHANG[1,*]

[1]School of Mechanical Engineering, Purdue University, West Lafayette, IN 47907, USA
[2]Department of Electronic Engineering, Tsinghua University, Beijing 100084, China
[*]szhang15@purdue.edu

Abstract: This paper presents a calibration method for a microscopic structured light system with an extended depth of field (DOF). We first employed the focal sweep technique to achieve large enough depth measurement range, and then developed a computational framework to alleviate the impact of phase errors caused by the standard off-the-shelf calibration target (black circles with a white background). Specifically, we developed a polynomial interpolation algorithm to correct phase errors near the black circles to obtain more accurate phase maps for projector feature points determination. Experimental results indicate that the proposed method can achieve a measurement accuracy of approximately 1.0 μm for a measurement volume of approximately 2,500 μm (W) × 2,000 μm (H) × 500 μm (D).

1. Introduction

With recent advances in technical fields, such as precision manufacturing and micro-robotics, applications of microscopic three-dimensional (3D) metrology approaches have attracted extensive attention [1–3]. Although being commonly used in macro scale, the structured light (SL) system with fringe projection technique is regarded as one of the most important methods owing to its high speed, high resolution, and high accuracy [4].

However, to migrate the SL approach to micro scale, the small depth-of-field (DOF) problem becomes especially fatal when pin-hole lenses are used because the DOF of the system is usually too shallow to complete 3D measurement at one time in many applications [5]. An alternative solution for this problem is to use telecentric lenses because of their unique properties of invariant magnification, low distortion, and increased DOF [6,7]. For telecentric lenses, 3D reconstruction strategies for such SL systems can be categorized into two groups: vertical scanning methods and triangulation-based methods.

The vertical scanning methods have attracted some attention owing to their unique shadow-free advantage which is beneficial for reconstructing scenes where depth geometry varies drastically. Zhong et al. [8] proposed an uni-axial microscopic 3D profilometry based on modulation measuring. Zheng et al. [9] analyzed the relationship between depth and fringe pattern defocus and proposed an active shape from projection defocus profilometry. Despite many advantages, vertical scanning methods usually require a time-consuming system setup because camera and projector have to be optically uni-axial.

In triangulation-based methods, calibration is one of the most important steps in order to achieve high accurate 3D measurement. However, due to the property of orthogonal projection, the existing calibration method for pin-hole camera proposed by Zhang [10] cannot be directly applied to telecentric optics. Consequently, several calibration methods for SL systems with telecentric lenses have been studied. Li and Tian [5,7] proposed a two-step calibration approach for a camera with a telecentric lens and then successfully employed the approach to a SL system with dual telecentric lenses. Li and Zhang [11] proposed a fast and flexible calibration method

#448019 https://doi.org/10.1364/OE.448019
Journal © 2022 Received 8 Nov 2021; revised 11 Dec 2021; accepted 14 Dec 2021; published 20 Dec 2021

Optics EXPRESS

for SL systems consisting of a camera with a telecentric lens and a projector with a pin-hole lens. Although these methods work well, the DOF of the systems only relies on the telecentric lenses without any extension.

In 2D imaging, some computational methods of extending DOF have raised interests in recent years such as coded aperture [12,13], wavefront coding [14,15], focal stack [16–18], and focal sweep [19,20], etc. Among these methods, the focal sweep technique has shown some potential to be applied to SL systems. Hu et al. [21] utilized an electrical tunable lens (ETL) to implement focal sweep technique in a SL system to realize a large DOF. However, such a method was only applied to a macro scale SL system and its performance under micro scale has not been fully evaluated.

It is well known that it is desirable to use a target with white feature points for structured light system calibration. However, it is increasingly difficult to find a standard calibration target with white circles as the system magnification increases. As such, it is more desirable to use a calibration target with a black circles grid because it is much easier to find such an off-the-shelf and precisely manufactured calibration target. However, our research found that the phase error problem introduced by the black circles has to be resolved before this kind of calibration target can be used for microscopic system calibration.

This research proposes a calibration method for a microscopic SL system to achieve a large DOF. The proposed method first uses a focal sweep technique to extend the DOF of the system. Then, a polynomial interpolation method is proposed to solve the phase error problem when using an off-the-shelf calibration target with black circles. Combining these with the basic principles of the existing SL system calibration algorithm proposed by Zhang and Huang [22], the system can be accurately calibrated. Experiments show that the proposed method can achieve high accuracy for a large measurement volume.

The rest of the paper is organized as follows. Section 2 explains the design of the proposed SL system and the principles of calibrating such a system. The Section 3 shows the experiments and results for evaluating performance of the proposed method, and Section 4 summarizes this paper.

2. Principles

This section discussed the principles behind the proposed technology as well as the desire to design a different microscopic SL system.

2.1. System configuration

A conventional SL system consisting of a camera and a projector can be illustrated as Fig. 1. The camera and the projector directly capture or project images from two perspectives. In a micro-scale application that is required to capture micrometer spatial resolution, both the camera and the projector require a large magnification. From geometric optics, the magnification of an optical imaging system can be increased by expanding the image distance,

$$\beta = \frac{s'}{s}, \tag{1}$$

where s' is the image distance and s is the object distance. In this case, some extension tubes can be mounted to the camera and the projector to expand image distance. However, from the lens equation,

$$\frac{1}{s} + \frac{1}{s'} = \frac{1}{f}, \tag{2}$$

where f is the focal length, it can be found that the object distance(i.e., working distance) will be reduced, meaning that the object has to be placed very close to the system during the imaging process. On the other hand, the field-of-view (FOV) will also be limited due to the big

Optics EXPRESS

magnification. Hence, due to mechanical interference or occlusion caused by the limited working distance and FOV, it is difficult to construct conventional SL system setup.

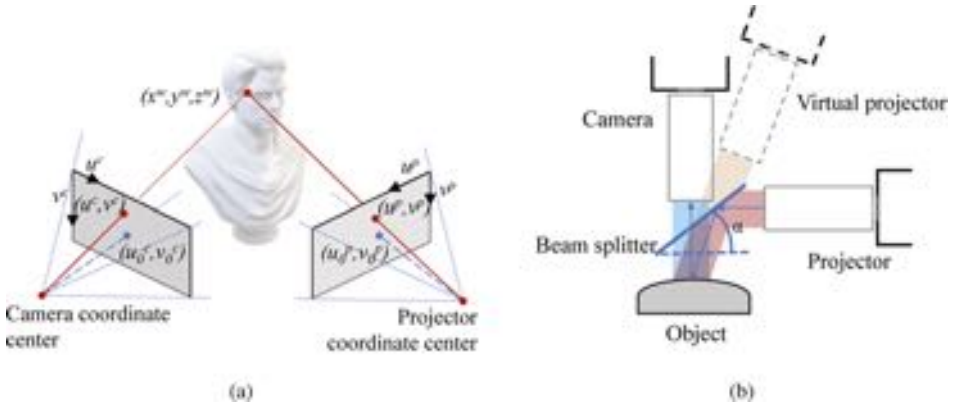

Fig. 1. SL system designs. (a) Conventional system and pin-hole model design. (b) Proposed microscopic system design.

To address this problem, a modified SL system configuration is designed, as shown in Fig. 1(b). A beam splitter is used to reflect light emitted from the projector. The reflected light can be considered as equivalent light from a virtual projector. Therefore, the modified configuration can be analyzed in the same way as the conventional SL system.

2.2. Pin-hole lens model

The pin-hole lens model is a widely used model describing the geometrical relationship of the camera imaging process. As shown in Fig. 1, the relationship between a point $P(x^w, y^w, z^w)$ on the object's surface and its projection point $P'(u^c, v^c)$ on the image sensor without considering lens distortions can be written as,

$$s^c \left[u^c, v^c, 1\right]^T = A^c \cdot \left[\mathbf{R}^c, \mathbf{t}^c\right] \cdot \left[x^w, y^w, z^w, 1\right]^T, \tag{3}$$

with

$$A^c = \begin{bmatrix} f_u & 0 & u_0 \\ 0 & f_v & v_0 \\ 0 & 0 & 1 \end{bmatrix}, \tag{4}$$

where s^c is a scaling factor, $[u^c, v^c, 1]^T$ is the homogeneous coordinate of an image pixel, A is a 3×3 matrix which is called intrinsic matrix, f_u and f_v are the focal length along u and v directions, u_0 and v_0 are coordinates of the camera center, $\mathbf{R}^c$ is a 3×3 rotation matrix, $\mathbf{t}^c$ is a 3×1 translation vector, and $[x^w, y^w, z^w, 1]^T$ is the homogeneous world coordinate of an object point. Similarly, since a projector can be considered as the inverse of a camera [22], it follows the same relationship,

$$s^p \left[u^p, v^p, 1\right]^T = A^p \cdot \left[\mathbf{R}^p, \mathbf{t}^p\right] \cdot \left[x^w, y^w, z^w, 1\right]^T, \tag{5}$$

where the superscript p denotes the projector's parameters.

Optics EXPRESS

In high accurate SL systems, lens distortions have to be taken into account. The lens distortions can be modeled as,

$$\begin{bmatrix} u_d \\ v_d \end{bmatrix} = (1 + k_1 r^2 + k_2 r^4 + k_3 r^6) \begin{bmatrix} \overline{u} \\ \overline{v} \end{bmatrix} + \begin{bmatrix} 2p_1\overline{uv} + p_2(r^2 + 2\overline{u}^2) \\ 2p_2\overline{uv} + p_1(r^2 + 2\overline{v}^2) \end{bmatrix}, \tag{6}$$

where $[k_1, k_2, k_3]$ are the radial distortion coefficients and $[p_1, p_2]$ are the tangential distortion coefficients; $[u_d, v_d]^T$ is the distorted coordinate and $[\overline{u}, \overline{v}]^T$ is the normalized coordinate. In practice, we only consider radial distortions, which means p_1 and p_2 equal 0.

2.3. Depth of field extension

As discussed previously, the object distance of the system is reduced in order to obtain a large magnification. It also brings a challenge to the DOF of a system. From the DOF formula in geometric optics,

$$D = \frac{2f^2 F\delta L(L-f)}{f^4 - F^2\delta^2(L-f)^2}, \tag{7}$$

where f is the focal length, F is the f-number, δ is the diameter of circle of confusion and L is the object distance. It is obvious that the DOF of the microscopic SL system is limited because L is small. Therefore, the DOF has to be extended for practical applications.

The focal sweep technique is one of the computational imaging methods to extend DOF without drastically reducing imaging speed. The degraded imaging process(i.e., image blurring) of a camera can be modeled as,

$$g = h \otimes i + \eta, \tag{8}$$

where g is the measured image; h is the point spread function (PSF) of the camera; i is the ideal image; and η is the noise. The notation $\otimes$ represents convolution.

In a conventional camera, the PSF can usually be approximately modeled as a Gaussian function which is variant to depth. Kuthirummal et al. [23] proved that when the focus is quickly swept over a depth range during an exposure process, an integrated PSF (IPSF) of the camera in this range is nearly invariant to depth. Therefore, the ideal image can be restored by deconvolution of Eq. (8). In this research, the Wiener Deconvolution algorithm is adopted which can be represented as,

$$\hat{I}(u,v) = \left[\frac{1}{H(u,v)} \frac{|H(u,v)|^2}{|H(u,v)|^2 + S_\eta(u,v)/S_f(u,v)}\right] G(u,v), \tag{9}$$

where $\hat{I}(u,v)$ is the Fourier transform of estimated restored image, $H(u,v)$ is the Fourier transform of the IPSF, $G(u,v)$ is the Fourier transform of a measured image and $S_\eta(u,v)/S_f(u,v)$ is the noise-to-signal ratio which can be set as a constant here.

In order to change the focus setting quickly, an electrical tunable lens (ETL) and its driving scheme proposed by Hu et al. [21] are adopted. The IPSF can be computed by,

$$h(x,y) = \int_{\sigma_l}^{\sigma_h} \frac{1}{2\pi\sigma^2} e^{-\frac{x^2+y^2}{2\sigma^2}} d\sigma + \int_{\sigma_h}^{\sigma_l} \frac{1}{2\pi\sigma^2} e^{-\frac{x^2+y^2}{2\sigma^2}} d\sigma, \tag{10}$$

where σ_l and σ_h are standard deviations which can be adjusted in experiments. Once the IPSF is obtained, Eq. (9) can be used to restore all-in-focus images. Figure 2 shows an example of applying the focal sweep technique to extend the DOF.

Optics EXPRESS

Fig. 2. Example of focal sweep technique for DOF extension. (a) Focus setting 1. (b) Focus setting 2. (c) Change focus setting during exposure from setting 1 to setting 2. (d) Restored all-in-focus image.

2.4. Multi-step phase-shifting algorithm

Phase-shifting algorithms are widely employed in SL systems because of their high accuracy, high resolution and high speed. The intensity of the k-th pattern for an N-step phase-shifting algorithm can be described as,

$$I_k(x,y) = I'(x,y) + I''(x,y)\cos[\phi(x,y) + 2k\pi/N], \tag{11}$$

where $I'(x,y)$ denotes the average intensity, $I''(x,y)$ is the intensity modulation amplitude, $\phi(x,y)$ is the phase to be solved, If $N \geq 3$, the unknown phase can be computed by,

$$\phi(x,y) = -\tan^{-1}\frac{\sum_{k=1}^{N} I_k(x,y)\sin(2k\pi/N)}{\sum_{k=1}^{N} I_k(x,y)\cos(2k\pi/N)}. \tag{12}$$

The phase map produced by the above equation is wrapped within a range from $-\pi$ to π with 2π discontinuities because of the nature of arctangent function. Hence, a temporal, spatial or alternative phase unwrapping algorithm which has been extensively studied over past few decades [24–26] is needed to recover a continuous phase map,

$$\Phi(x,y) = \phi(x,y) + 2\pi \times \kappa(x,y), \tag{13}$$

where κ(x,y) is an integer number obtained from the phase unwrapping algorithm. In this research, a three-frequency phase unwrapping algorithm is adopted.

2.5. Phase map correction

For a traditional SL system calibration, targets with white circles and a black background is preferable because high quality phases in dot regions can be obtained from the phase-shifting algorithm. However, as mentioned in Section 1, it is difficult to find a standard off-the-shelf calibration target with white circles for microscopic system calibration. Hence, using a standard calibration target black circles is preferable. But the problem of using black circles is that the phase cannot be accurately recovered near the edge of and inside the black circle areas, as shown in Fig. 3(a) and Fig. 3(b). Figure 3(c) shows the mapped projector feature points if the original phase maps are used [27]. It is obvious that the mapping is wrong. These incorrectly mapped projector feature points lead to incorrect projector and thus system calibration.

The phase errors mentioned above are introduced by the low fringe contrast inside black circle areas and high texture contrast near circle edges. With prior knowledge that the absolute phase map for each pose is expected to be smooth in a local window, we developed a computational framework to alleviate this problem.

The first step is to define each local windows. In this research, we created each local window using the detected feature points (i.e., circles center). The window for each circle is centered

Optics EXPRESS

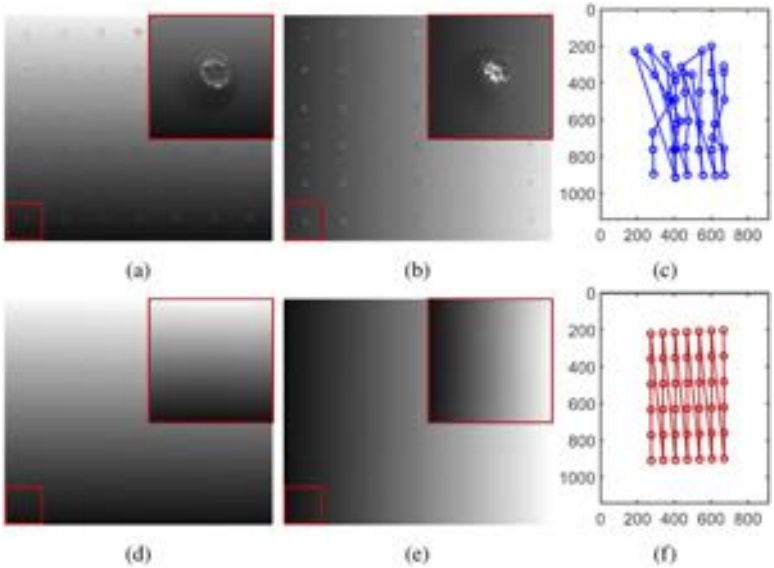

Fig. 3. Phase maps and corresponding projector feature points determination. (a)-(b) Original phase maps with phase errors inside and near the edge of black circles. (c) Mapped projector feature points using phase maps shown in (a)-(b). (d)-(e) Corrected phase maps after applying the proposed correction method. (f) Mapped projector feature points using phase maps shown in (d)-(e).

with the corresponding feature point, and the window size is dynamically determined as half of the distance to its nearest neighbor. Note that the window size for the circles around the image margins may be reduced considering the image size. Figure 4 shows an example of all local windows.

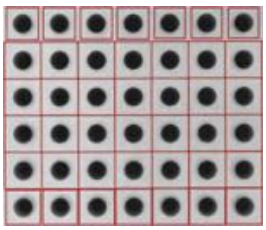

Fig. 4. Local windows generation. Each window center coincides with the circle center, and the windows size is dynamically determined as the half the distance to its nearest neighbor. The red rectangles in the figure represent the local windows.

Once each local window is defined, we developed the following two-stage polynomial fitting method to remove phase errors.

- *Stage 1*: for each column in each horizontal fringe phase map and for each row in each vertical fringe phase map, fit a polynomial function for those phase points in the white background area. In this research, the third-order polynomial is used, which can be represented as,

$$\Phi'_h(y) = a_3y^3 + a_2y^2 + a_1y + a_0, \tag{14}$$

$$\Phi'_v(x) = b_3x^3 + b_2x^2 + b_1x + b_0, \tag{15}$$

Optics EXPRESS

where a_0 to a_3, and b_0 to b_3 are polynomial coefficients. Figure 5 shows an example of fitting the horizontal and vertical phase maps. After the curve fitting, a new phase for each pixel in each row or column can be generated by comparing the original phase value and fitted phase value. If the difference between original phase value and fitted phase value exceeds a threshold, then the original phase value is replaced by the fitted value as the new phase value. It can be represented as:

$$\hat{\Phi}_h(x,y) = \begin{cases} \Phi_h(x,y) & |\Phi_h(x,y) - \Phi'_h(x,y)| < threshold \\ \Phi'_h(x,y) & |\Phi_h(x,y) - \Phi'_h(x,y)| > threshold \end{cases}, \tag{16}$$

and

$$\hat{\Phi}_v(x,y) = \begin{cases} \Phi_v(x,y) & |\Phi_v(x,y) - \Phi'_v(x,y)| < threshold \\ \Phi'_v(x,y) & |\Phi_v(x,y) - \Phi'_v(x,y)| > threshold \end{cases}, \tag{17}$$

where $\hat{\Phi}_h(x,y)$ and $\hat{\Phi}_v(x,y)$ represent the generated new phase values for horizontal and vertical fringe. $\Phi_h(x,y)$ and $\Phi_v(x,y)$ represent the original phase values and $\Phi'_h(x,y)$ and $\Phi'_v(x,y)$ represent the fitted phase values.

- *Stage 2*: run a polynomial surface fitting for each fringe direction using the updated phase values. In this research, a fourth-order polynomial surface fitting is used, which can be described as,

$$\hat{\Phi}'(x,y) = \sum_{m=0}^{4} \sum_{n=0}^{4-m} p_{mn} x^m y^n, \tag{18}$$

where p_{mn} are coefficients. The phase maps after correction and corresponding projector feature points determination are shown in Fig. 3(d)–Fig. 3(f).

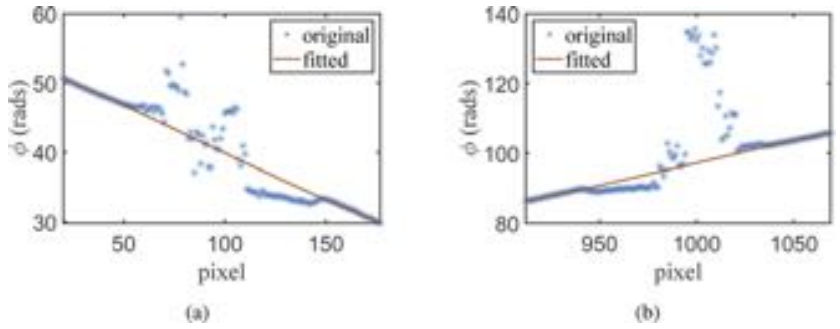

Fig. 5. Example of polynomial fitting for each row and column. (a) Curve fitting in horizontal fringe phase map. (b) Curve fitting in vertical fringe phase map.

2.6. Overall proposed computational framework

Figure 6 summarizes the computational framework of our proposed microscopic SL system calibration method. The whole procedure follows the basic flow of the existing SL calibration method proposed by Zhang and Huang [22] but introduces the focal sweep technique and phase error correction method, discussed in Section 2. In this research, a three-frequency phase unwrapping algorithm is used for phase extraction. The steps of the three frequency fringes from highest to lowest are 9, 3, 3 with fringe pitches of 36, 216, 1140 pixels respectively for the horizontal direction, and 18, 144, 912 pixels respectively for the vertical direction.

Optics EXPRESS

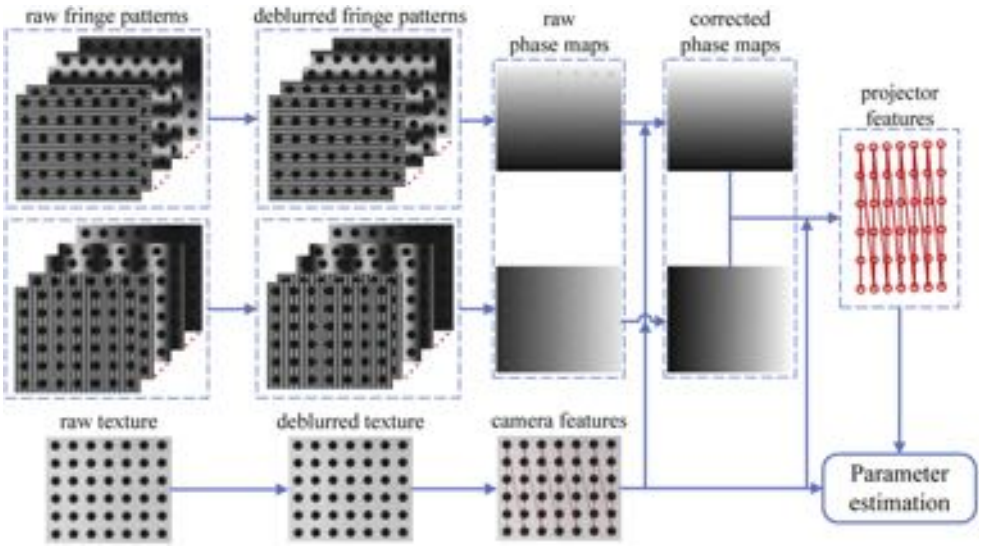

Fig. 6. Proposed computational framework for our proposed calibration method. All captured images with the focal sweep technique including fringe images and texture images are first deblurred. The texture image is further used to extract feature points (i.e., black circles centers) and those fringe images are used to compute phase maps. Those raw phase maps are further processed to reduce phase errors using the proposed phase error reduction method. The corrected phase are used to determine corresponding projector feature points for those camera feature points. Finally, the camera and projector parameters are estimated using camera and projector feature points.

3. Experiments

A prototype system shown in Fig. 7 was developed to evaluate the performance of our proposed calibration method. A complementary metal-oxide-semiconductor (CMOS) camera (model: PointGrey GS3-U3-23S6M) was attached with a lens system consisting of a 35 mm fixed aperture (f/1.6) lens (model: Edmund Optics #85-362), an equivalent 20 mm extension tube, a circular polarizer (model: Edmund Optics CP42HE), and an ETL (model: Optotune EL-16-40-TC). Note that the lens was mounted reversely to increase image distance. A digital-light-processing (DLP) projector (model: Shanghai Yiyi D4500) was equipped with a lens system composed of a 35 mm lens (model: Fujinon HF35HA-1B), a circular polarizer (model: Edmund Optics CP42HE) and an ETL (model: Optotune EL-16-40-TC). Each ETL in this system was tuned by a lens driver controller (model: Optotune Lens Driver 4i) from -2 to +3 dpt. A beam splitter (model: Thorlabs BP145B1) was used to address hardware constraints. The camera and the projector were synchronized by a microprocessor (model: Arduino Uno). Due to the limited FOV, only 6×7 circles in the calibration target (model: Edumund Optics #62-953) were used for both calibration and measurement.

For all the following experiments, the camera resolution was set as 1280×1080 pixels and the projector resolution was 912×1140 pixels. The driving signal for the ETL in the camera lens system was set as a 100 Hz triangular wave oscillating within an interval of -125.15 mA to -100.19 mA. The driving current of the ETL in projector lens system was set as 30.03 mA. The aperture of the projector lens was set as f/4.0.

We first evaluated the random noise level of the system by measuring a flat plane (i.e., a pure white area of the calibration target). The reconstructed point cloud data was compared against a fitted ideal plane to generate an error map. Figure 8(a) shows the error along a row

Optics EXPRESS

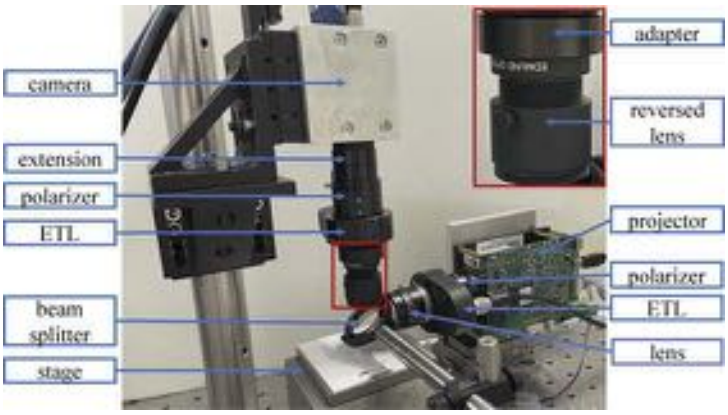

Fig. 7. Photograph of our prototype system.

in the generated error map. The random noise was calculated by removing the overall trend of the signal shown Fig. 8(a). Figure 8(b) shows the random noise. The root-mean-square error (RMSE) of the random noise was 1.67 μm. The most significant noise can be further suppressed by applying a small Gaussian filter (size of 5×5 pixels and standard deviation of $\sigma = 1.67$ pixel) to the unwrapped phase. For the rest of the paper, the same Gaussian filter was applied to all data. Figure 8(c) shows the result after applying the Gaussian filter, and the RMSE dropped down to 0.62 μm. This RMSE can be considered as a reference for the depth resolution.

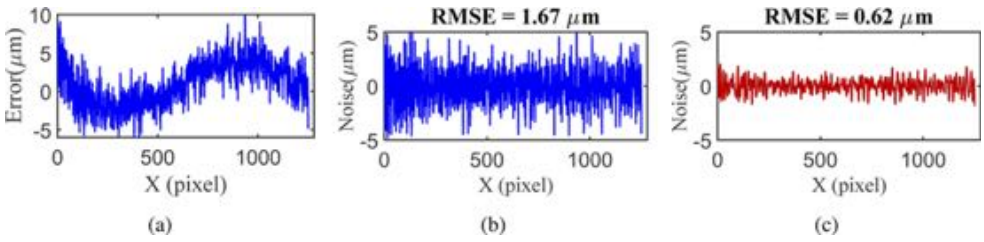

Fig. 8. Random noise evaluation by measuring a flat plane. (a) The error along a row in the generated error map. (b) Random noise after removing the overall profile shown in (a). (c) The random noise after applying a 5×5 Gaussian filter.

We then measured the length of two diagonals (i.e., $\overline{AC}$ and $\overline{BD}$ shown in Fig. 9) of the calibration target in different poses (shown in Fig. 9(b)) from the reconstructed 3D point cloud data. Due to the phase error problem mentioned in Section. 2.5, the coordinates of the black circles cannot be accurately reconstructed, so the diagonals were formed by centers of neighboring four circles, which are shown in Fig. 9(a). The reference value of the length can be simply calculated by the circles spacing. For the calibration target we used here, the length of the diagonal is $\sqrt{41}d$ where d is the spacing. The measurement error is the difference between the measured distance and the reference value. Table 1 summarizes the results. These measurement indicated that the error is very small: an average of approximately 1 μm and standard deviation of approximately 0.7 μm for a measurement volume of 2,500 μm (W) × 2,000 μm (H) × 500 μm (D). This is very small considering that each camera pixel is approximately 2.7 μm in the object space.

To further evaluate the depth measurement accuracy, we put a flat plane (i.e., same as the first experiment) on a precision vertical translation stage (model: Newport M-MVN80) and move the plane to different heights with an increment of 25 μm. The reconstructed 3D results and a

Optics EXPRESS

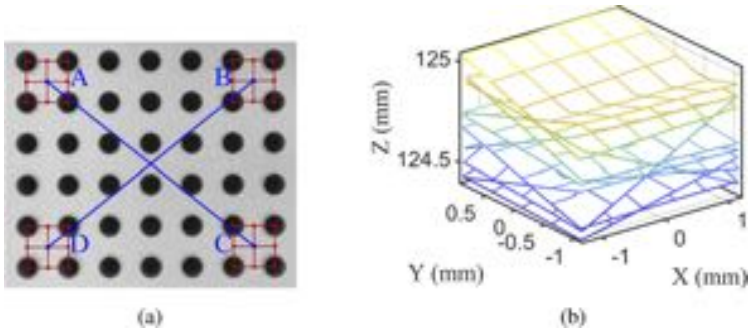

Fig. 9. Diagonal measurements of a flat surface at different poses. (a) Measured diagonals. (b) Measured poses of the target.

Table 1. Measurement of two diagonals in calibration target (in μm). The pose plane function is defined as $z = a + bx + cy$.)

[a, b, c]	$\overline{AC}$ Error	$\overline{BD}$ Error
[98.9645, -1.4540, -3.7811	0.82	0.12
[99.0669, -1.4964, -3.7854]	0.69	0.97
[99.8014, -1.5012, -3.6768]	2.30	1.18
[99.2229, -1.5552, -3.9535]	0.49	1.56
[99.7896, -1.2965, -3.8682]	1.45	1.19
[99.2675, -1.6459, -4.1349]	0.69	1.41
[99.2063, -1.7157, -4.3335]	1.34	0.45
[99.0308, -1.5665, -3.8817]	1.85	1.32
[99.1863, -1.7463, -3.5655]	0.16	0.05
[99.1009, -1.7899, -3.6317]	1.01	2.26
Mean	1.08	1.05
RMS	0.65	0.68

cross section are shown in Fig. 10(a) and Fig. 10(b). We calculated a rigid translation $\mathbf{t}_i$ against the first measurement along the Z-axis, where i denotes the i-th stage position. The translation was calculated by an average distance over a 9×9 window aligned with the camera center, then it was compared with the actual stage translation. Figure 10(c) shows that the mean depth error is approximately 1.02 μm, which is again quite small compared with the overall 475 μm translation range (approximately 0.2%).

A 3D object with complex geometry was measured to visually demonstrate the performance of our proposed calibration method. The object was a part of a M3-0.5 screw as shown in Fig. 11(a). Figure 11(b) shows one of the raw fringe patterns, and Fig. 11(c) shows the corresponding deblurred fringe pattern. The recovered wrapped phase map and unwrapped phase map are shown in Fig. 11(d) and Fig. 11(e), respectively. Figure 11(f) shows the geometry of the reconstructed 3D model. One vertical cross section is shown in Fig. 11(g). This experiment visually demonstrated the proposed method works well.

Optics EXPRESS

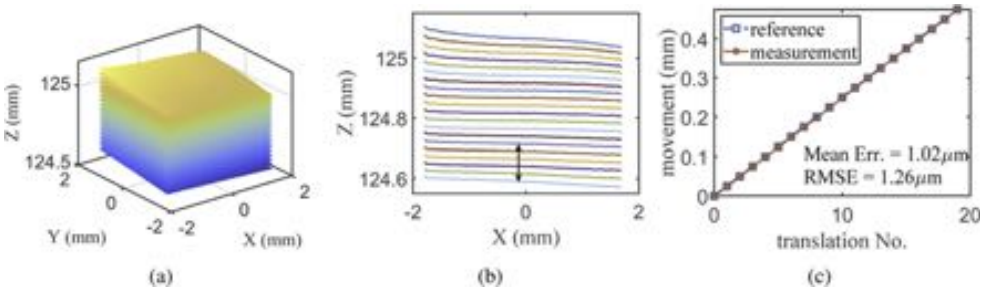

Fig. 10. Vertical translation measurements. (a). Reconstructed 3D results of the vertical translated flat planes. (b) The cross sections of (a). (c) Comparison between the measured translation and actual translation. The mean error was 1.02 μm and the RMSE was 1.26 μm.

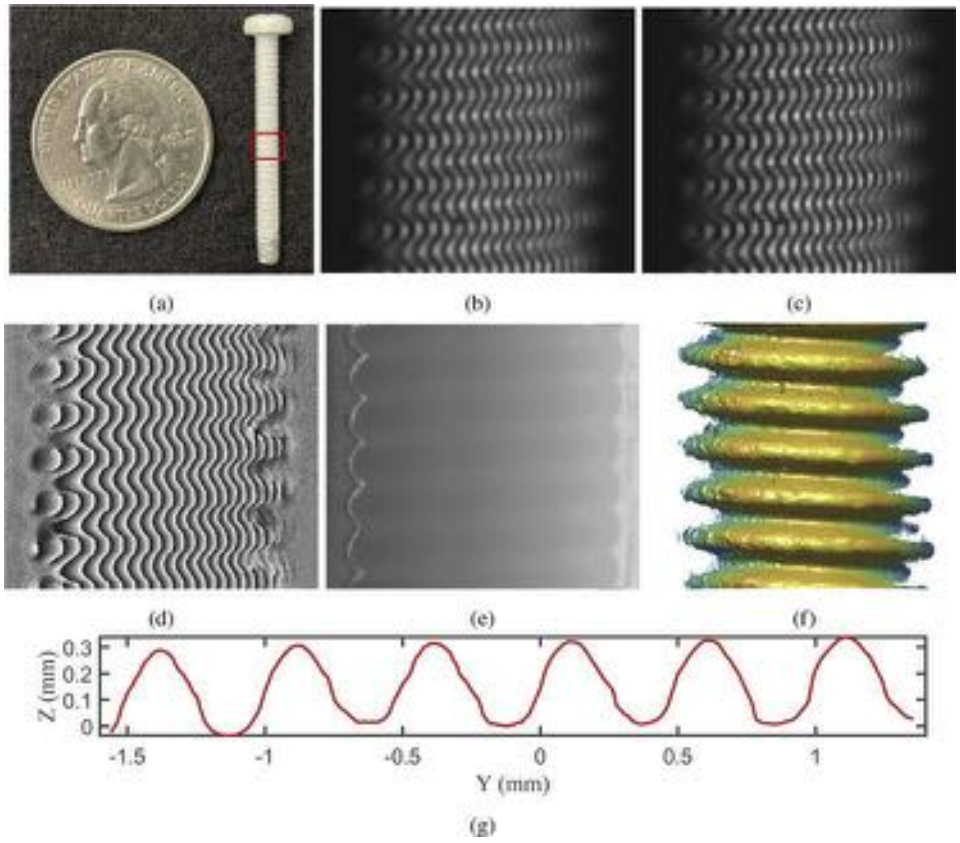

Fig. 11. 3D reconstruction of a M3-0.5 screw. (a) Photograph of the object. (b) One of the captured high frequency fringe pattern. (c) Deblurred image of (b). (d) Wrapped phase map. (e) Unwrapped phase. (f) Reconstructed 3D model. (g) One cross section of the reconstructed 3D model.

Optics EXPRESS

4. Summary

This paper presents a calibration method for a microscopic SL system with extended depth of field (DOF) using a standard calibration target. The proposed approach enables SL systems to be used in more microscopic 3D measurement applications. It extended the DOF by employing the focal sweep technique, and made the calibration method more flexible by allowing the use of a black circles grid calibration target. Experimental results indicate that the proposed method can achieve a measurement accuracy of approximately 1 μm for a measurement volume of approximately 2,500 μm (W) × 2,000 μm (H) × 500 μm (D).

Funding. Directorate for Computer and Information Science and Engineering (IIS-1763689).

Disclosures. LC: The author declares no conflicts of interest. XWH: The author declares no conflicts of interest. SZ: ORI LLC (C), Orbbec 3D (C), Vision Express Optics Inc (I).

Data availability. Data underlying the results presented in this paper are not publicly available at this time but may be obtained from the authors upon reasonable request.

References

1. S. S. Gorthi and P. Rastogi, "Fringe projection techniques: Whither we are?" Opt. Lasers Eng. **48**(2), 133–140 (2010).
2. S. Zhang, "Recent progresses on real-time 3d shape measurement using digital fringe projection techniques," Opt. Lasers Eng. **48**(2), 149–158 (2010).
3. S. Zhang, *High-Speed 3D Imaging with Digital Fringe Projection Techniques* (CRC, Inc., USA, 2016).
4. Y. Hu, Q. Chen, S. Feng, and C. Zuo, "Microscopic fringe projection profilometry: A review," Opt. Lasers Eng. **135**, 106192 (2020).
5. D. Li, C. Liu, and J. Tian, "Telecentric 3d profilometry based on phase-shifting fringe projection," Opt. Express **22**(26), 31826–31835 (2014).
6. J. Kim and T. Kanade, "Multi-aperture telecentric lens for 3d reconstruction," Opt. Lett. **36**(7), 1050–1052 (2011).
7. D. Li and J. Tian, "An accurate calibration method for a camera with telecentric lenses," Opt. Lasers Eng. **51**(5), 538–541 (2013).
8. M. Zhong, J. Cui, J.-S. Hyun, L. Pan, P. Duan, and S. Zhang, "Uniaxial three-dimensional phase-shifting profilometry using a dual-telecentric structured light system in micro-scale devices," Meas. Sci. Technol. **31**(8), 085003 (2020).
9. Y. Zheng, Y. Wang, and B. Li, "Active shape from projection defocus profilometry," Opt. Lasers Eng. **134**, 106277 (2020).
10. Z. Zhang, "A flexible new technique for camera calibration," IEEE Trans. Pattern Anal. Machine Intell. **22**(11), 1330–1334 (2000).
11. B. Li and S. Zhang, "Flexible calibration method for microscopic structured light system using telecentric lens," Opt. Express **23**(20), 25795–25803 (2015).
12. A. Levin, R. Fergus, F. Durand, and W. T. Freeman, "Image and depth from a conventional camera with a coded aperture," ACM Trans. Graph. **26**(3), 70 (2007).
13. A. Veeraraghavan, R. Raskar, A. Agrawal, A. Mohan, and J. Tumblin, "Dappled photography: Mask enhanced cameras for heterodyned light fields and coded aperture refocusing," ACM Trans. Graph. **26**(3), 69 (2007).
14. E. R. Dowski and W. T. Cathey, "Extended depth of field through wave-front coding," Appl. Opt. **34**(11), 1859–1866 (1995).
15. N. George and W. Chi, "Extended depth of field using a logarithmic asphere," J. Opt. **5**(5), S157–S163 (2003).
16. S. W. Hasinoff and K. N. Kutulakos, "Light-efficient photography," IEEE Trans. Pattern Anal. Machine Intell. **33**(11), 2203–2214 (2011).
17. S. W. Hasinoff, K. N. Kutulakos, F. Durand, and W. T. Freeman, "Time-constrained photography," in *2009 IEEE 12th International Conference on Computer Vision*, (2009), pp. 333–340.
18. S. Suwajanakorn, C. Hernandez, and S. M. Seitz, "Depth from focus with your mobile phone," in *2015 IEEE Conference on Computer Vision and Pattern Recognition (CVPR)*, (2015), pp. 3497–3506.
19. S. Liu and H. Hua, "Extended depth-of-field microscopic imaging with a variable focus microscope objective," Opt. Express **19**(1), 353–362 (2011).
20. D. Miau, O. Cossairt, and S. K. Nayar, "Focal sweep videography with deformable optics," in *IEEE International Conference on Computational Photography (ICCP)*, (2013), pp. 1–8.
21. X. Hu, S. Zhang, Y. Zhang, Y. Liu, and G. Wang, "Large depth-of-field three-dimensional shape measurement with the focal sweep technique," Opt. Express **28**(21), 31197–31208 (2020).
22. S. Zhang and P. S. Huang, "Novel method for structured light system calibration," Opt. Eng. **45**(8), 083601 (2006).
23. S. Kuthirummal, H. Nagahara, C. Zhou, and S. Nayar, "Flexible Depth of Field Photography," IEEE Trans. Pattern Anal. Machine Intell. **99**, 1 (2010).
24. C. Zuo, L. Huang, M. Zhang, Q. Chen, and A. Asundi, "Temporal phase unwrapping algorithms for fringe projection profilometry: A comparative review," Opt. Lasers Eng. **85**, 84–103 (2016).

Optics EXPRESS

25. X. Su, "Phase unwrapping techniques for 3D shape measurement," in *International Conference on Holography and Optical Information Processing (ICHOIP '96)*, G. Mu, G. Jin, and G. T. Sincerbox, eds., International Society for Optics and Photonics (SPIE, 1996).
26. S. Zhang, "Absolute phase retrieval methods for digital fringe projection profilometry: A review," Opt. Lasers Eng. **107**, 28–37 (2018).
27. B. Li, N. Karpinsky, and S. Zhang, "Novel calibration method for structured-light system with an out-of-focus projector," Appl. Opt. **53**(16), 3415–3426 (2014).